

Automatic Defect Detection on Hot-Rolled Flat Steel Products

Santanu Ghorai, *Member, IEEE*, Anirban Mukherjee, *Member, IEEE*, M. Gangadaran, and Pranab K. Dutta, *Member, IEEE*

Abstract—Automatic defect detection on hot-rolled steel surface is challenging owing to its localization on a large surface, variation in appearance, and their rare occurrences. It is difficult to detect these defects either by physics-based models or by small-sample statistics using a single threshold. As a result, this problem is focused to derive a set of good-quality defect descriptors from the surface images. These descriptors should discriminate the various surface defects when fed to suitable machine learning algorithms. This research work has evaluated the performance of a number of different wavelet feature sets, namely, Haar, Daubechies 2 (DB2), Daubechies 4 (DB4), biorthogonal spline, and multiwavelet in different decomposition levels derived from 32×32 contiguous (nonoverlapping) pixel blocks of steel surface images. We have developed an automated visual inspection system for an integrated steel plant to capture surface images in real time. It localizes defects employing kernel classifiers, such as support vector machine and recently proposed vector-valued regularized kernel function approximation. Test results on 1000 defect-free and 432 defective images comprising of 24 types of defect classes reveal that three-level Haar feature set is more promising to address this problem than the other wavelet feature sets as well as texture-based segmentation or thresholding technique of defect detection.

Index Terms—Automated visual inspection system, defect detection, discrete wavelet transform (DWT), kernel classifier, support vector machine (SVM).

I. INTRODUCTION

QUALITY control is an important aspect of all industrial production. In recent years, many automated manpower saving systems have been developed (and employed) to reduce the production cost and improve the quality of steel products. However, in the finishing product, quality assurance with respect to surface defects is partly automated and mostly

performed by manual inspection. The global economic development has gradually led steel production industries to increase its production rate ensuring simultaneously stringent limit on the quality of product. In order to meet the growing demand for high-quality product in short duration, the use of intelligent visual inspection systems is increasingly essential in production lines. The use of automated inspection technique is necessary at each level of production to improve the quality of product as well as to eliminate the need of a human intervention in a hazardous environment. This will facilitate to make the surface information available immediately after the rolling process. This has an obvious benefit in terms of quality assurance. The surface defects often arise as a result of systematic process problems, such as (partially) damaged machinery or metallurgical drift. Thus, the early detection of defects can also have a direct cost benefit in terms of saving of time as well as to prevent rejection from being generated in large quantities, in downstream.

In the literature, there are methods of defect detection inside steel casting [1], on fabric surface [2]–[4], glass plates [5], liquid crystal display images [6], etc. The defect detection in steel casting typically relies on X-ray image processing to localize any internal flaw. However, surface defect detection can be performed by processing the surface images [7]. Unfortunately, in the literature, there are a few research works for steel surface defect detection [8]–[11]. Most of the defect detection techniques are used in some commercially available systems. These are not reported in the literature due to the constraints in intellectual property right. In [8], Sugimoto and Kawaguchi described a system based on applied radiant light, and it senses the temperature deviation caused by defects. They described an inspection system of steel surface defects for large sections, such as wide-flange beams and I-beams. Among the recent works, Choi *et al.* [9] proposed an edge-preserving filter and thresholding technique to detect crack, spot, and dark line for high-speed steel bar in coil. An average accuracy of 95.42% has been achieved with this method. Solly and Smith [10] developed a rapidly reconfigurable system in which the users' tacit knowledge and requirements are elicited via a process of interactive evolution, finding the image processing parameters to achieve the required goals without any need for specialized knowledge of the machine-vision system. This offered satisfactory results only for scratches, rolled in scale, and bruise types of defects. Yong *et al.* [11] proposed an algorithm based on undecimated wavelet transform and mathematical morphology for detection of geometric defects, such as scratches and various cracks on hot-rolled steel plates. They achieved a recognition rate of up to 90.23% which is difficult to be appreciated for industrial

Manuscript received May 7, 2012; revised August 24, 2012; accepted August 28, 2012. Date of publication October 22, 2012; date of current version February 5, 2013. This work was supported in part by Department of Information Technology, Government of India. The Associate Editor coordinating the review process for this paper was Dr. Ruqiang Yan.

S. Ghorai is with the Department of Applied Electronics and Instrumentation Engineering, Heritage Institute of Technology, Kolkata 700107, India (e-mail: santanu.ghorai@heritageit.edu).

A. Mukherjee is with the Department of Electrical Engineering, Indian Institute of Technology Kharagpur, Kharagpur 721302, India (e-mail: anirban@ee.iitkgp.ernet.in).

M. Gangadaran is with the Appropriate Automation Promotion Centre Group, Research and Development for Iron and Steel, Steel Authority of India Ltd., Ranchi 834002, India (e-mail: mganga@sail-rdcis.com).

P. K. Dutta is with the Department of Electrical Engineering and the Head of the School of Medical Science and Technology, Indian Institute of Technology Kharagpur, Kharagpur 721302, India (e-mail: pkd@ee.iitkgp.ernet.in).

Color versions of one or more of the figures in this paper are available online at <http://ieeexplore.ieee.org>.

Digital Object Identifier 10.1109/TIM.2012.2218677

application. In recent years, machine learning algorithms are efficiently applied in many industries for automatic detection of faults [12]–[14] as well as for dynamic process monitoring [15].

There are certain major difficulties in defect detection of hot-rolled steel surface. These are as follows.

- 1) The classification of local area of surface defects on hot-rolled steel surface is a challenging task due to the variability in manifestations of the defects grouped under the same defect label. Surface defects of steel plates can be broadly categorized into two main groups: a) textural defects and b) geometric defects. Textural defects, such as heavy scale, rolled in scale, salt and pepper, slab edge, and so on, can be detected by the methods based on textural analysis. Geometric defects, such as cracks, scratches, etc., can be detected by algorithms based on morphological filtering. In addition, these defects on steel surface can be effectively identified from the uniform images with the small-sample statistics like the mean and variance of gray levels. They can also be detected using simple thresholding or edge-detection techniques. However, the large variety of defects requires different threshold values for different types of defects. However, a good defect detection system should detect all types of defects equally by the same algorithm.
- 2) There is a great deal of scales with different colors and appearances on the surface of steel plates, which makes the background detection task difficult.
- 3) In spite of careful arrangement of uniform illumination over the steel surface, the problem of vibration-induced uneven illumination is difficult to overcome. Therefore, a suitable defect detection algorithm of hot-rolled steel surfaces needs to be insensitive to scales and uneven illumination to the maximum possible extent.

This research work addresses to overcome the first two difficulties of the surface inspection system. This work demonstrates that a small set of wavelet features, when employed with kernel classifiers, can detect a wide variety of defects on steel surface. The set of wavelet features are extracted from small blocks of steel surface images. In order to obtain the digital images of the top surface of hot-rolled steel sheet in real time, an automated visual inspection system has been developed in a steel plant. The system comprises of both hardware and software customized for this application. Five different types of wavelets, namely, Haar, Daubechies 2 (DB2), Daubechies 4 (DB4), biorthogonal spline (Bior), and multiwavelet, have been used to extract features by decomposing the small blocks of surface images into different resolution levels, i.e., level 1, level 2, and level 3. The defect detection ability of these features along with texture segmentation or thresholding technique of defect detection is assessed by two kernel classifiers, namely, the support vector machine (SVM) classifier [16], [17] and the vector-valued regularized kernel function approximation (VVRKFA) method of classification [18]. We have applied these two classifiers on 24 different types of steel surface defects as well as on defect-free images. From the experimental study on various wavelet features with different resolution levels, it has been observed that the Haar wavelet feature with

three resolution levels is a promising candidate to address this problem. To the best of our knowledge, there is a little work available in the literature covering the detection of as many as 24 types of surface defect and their detection by a single classification algorithm using the proposed feature sets.

The remaining part of this paper is organized in the following way. Section II focuses on the different types of defect that appears on steel surface. In Section III, a brief theory of VVRKFA is described. In Section IV, the automated defect detection scheme (feature extraction, training of classifiers, experimental results, and timing requirements) is presented. Section V, finally, provides the conclusion of this research.

II. VARIOUS TYPES OF DEFECTS ON STEEL SURFACE

The nomenclature of surface defects on hot-rolled steel surface is generally cast by visual appearance of the defect texture or its geometry. The 24 types of steel surface defects are shown in the supplementary material file (see supplemental material, available at <http://ieeexplore.ieee.org>). Most of the divisions are subjective, and several can be grouped under the same label, e.g., scratches may be bright scratch, dark scratch, etc. These groupings are performed by practitioners, having rich experience in the steel plant. All these defects appear during hot-rolling process due to mechanical or metallurgical imperfection. With a careful observation, two principal types of defects are encountered with respect to the space localization: 1) local defect and 2) distributed defect. Local defects are limited in space but may appear in a discontinuous fashion on different places of the surface. For example, scratches, crack, rupture, blister, bruise, head mark, etc., belong to this category. On the other hand, distributed defects are spread (continuously) over the large area of the surface. For example, rolled in scale, salt and pepper, scale grain, and slab edge are categorized in this group. Local defect, being constrained in space, is principally the outcome of imperfect rolling. On the other hand, the distributed defect is mainly attributed to shortcomings in metallurgical mixing in upstream. Alternatively, the defects may be classified into two types based on appearance: 1) geometric defects such as scratches, cracks, head mark, rupture, spall, waviness, whip, etc., and 2) textural defects such as rolled in scale, salt and pepper, scales in grain, slab edge, etc.

Defect classification is as important as defect detection for gradation of the steel sheets because the usability and associated penalty posed by various utilities depend on both the amount of the defect and the type of defects. Moreover, due to disturbance created in the intensity profile, some of the water droplets and dirt are detected as defects or disturbances initially. These false alarms are reduced to a large extent in the defect classification stage. Instead of categorizing the defective samples in different classes, we, in this research, discriminate the defect-free samples from the defective ones.

III. MACHINE LEARNING ALGORITHMS

SVM [16], [17] is a well-known kernel classifier and has been widely used in almost all types of pattern classification applications. As a result, its description is omitted here. The

recently proposed VVRKFA method of classification is briefly described here. Interested readers may find an excellent explanation of SVM in [16] and [17].

The VVRKFA approach of classification is originally proposed for fast classification of large multiclass data set [18]. The decomposition techniques of multiclass data classification suffer from problems, like data unbalance, large training, and testing time, and, hence, parameter tuning for large data set. It is observed that VVRKFA improves over the limitations of decomposition techniques by reducing both computational and space complexity in case of large data sets. An additional advantage of VVRKFA method is that it may be useful for analyzing the degree of separability of the classes of a data set. Since the high-dimensional data are classified in a subspace equal to the number of class label, it can be used as data visualization tool if the number of classes is two or three. In this paper, we have chosen this scheme for binary data classification to profitably use its merits of computational complexities. This method of classification has three parts: coding, training, and decoding. For an N class problem, the label vector Y_i of a sample x_i of j th class is chosen as the indicator vector of the classes according to the following rule:

$$Y_i = [y_{1i}, y_{2i}, \dots, y_{Ni}]^T \text{ with } y_{ji} = 1 \text{ and } y_{ki} = 0 \text{ for } k \neq j \in N. \quad (1)$$

The VVRKFA is obtained on this training sample by the following optimization problem:

$$\begin{aligned} \text{Min } J(\Theta, b, \xi) &= \frac{C}{2} \text{tr}([\Theta \ b]^T [\Theta \ b]) + \frac{1}{2} \sum_{i=1}^m \|\xi_i\|^2 \\ \text{s.t. } \Theta k(x_i^T, B^T)^T + b + \xi_i &= Y_i, \quad i = 1, 2, \dots, m. \end{aligned} \quad (2)$$

Here, $\Theta \in \mathbb{R}^{N \times \bar{m}}$ is the regression coefficient matrix that maps the inner products of the feature space to the label space, and $b \in \mathbb{R}^{N \times 1}$ is the bias vector. C is a regularization parameter, and $\xi_i \in \mathbb{R}^{N \times 1}$ is the slack or error variable vector. The matrix $B \in \mathbb{R}^{\bar{m} \times n}$ contains the reduced training set; the dimension of the feature space is $\bar{m} (\leq m)$, and $k(\cdot, \cdot)$ is a kernel function [19]. By this method, \bar{m} numbers of patterns are selected randomly from the full data set prior to the training. These preselected patterns are used as the basis pattern to form the kernel matrix. Let the matrix $A \in \mathbb{R}^{m \times n}$ represent the training set. Then, the problem (2) reduces to an unconstrained minimization problem as

$$\begin{aligned} \min J(\Theta, b) &= \frac{C}{2} \text{tr}([\Theta \ b]^T [\Theta \ b]) \\ &+ \frac{1}{2} \left\| \Theta k(A, B^T)^T - b e^T - Y \right\|_F^2 \end{aligned} \quad (3)$$

where $Y \in \mathbb{R}^{N \times m}$ is the matrix containing m label vectors of the training data and $\|A\|_F$ is Frobenius norm [20] of any matrix $A \in \mathbb{C}^{p \times q}$ defined as $\|A\|_F = \sqrt{\sum_{i=1}^p \sum_{j=1}^q |a_{ij}|^2}$. Optimization problem (3) can be further simplified by substituting $\Omega = [\Theta \ b] \in \mathbb{R}^{N \times (\bar{m}+1)}$ in it as

$$\min J(\Omega) = \frac{C}{2} \text{tr}(\Omega^T \Omega) + \frac{1}{2} \|\Omega P - Y\|_F^2 \quad (4)$$

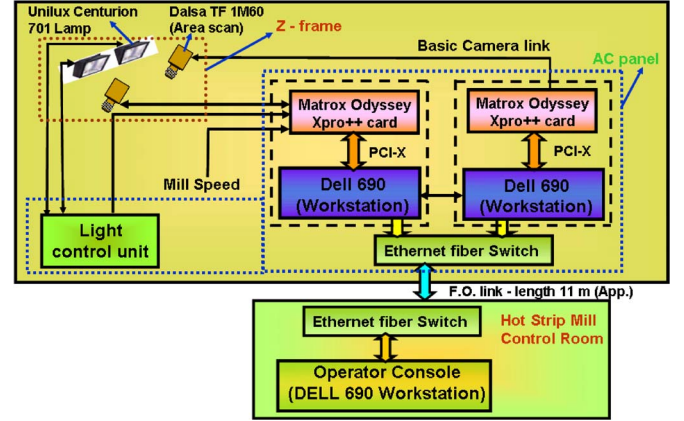


Fig. 1. Top surface inspection schematic.

where $P = [k(A, B^T)e]^T \in \mathbb{R}^{(\bar{m}+1) \times m}$ is augmented matrix. The unique global solution of the convex objective function (4) can be obtained by differentiating it with respect to Ω and equating it to zero (null matrix), i.e.,

$$\begin{aligned} \frac{d}{d\Omega} \left[\frac{C}{2} \text{tr}(\Omega^T \Omega) + \frac{1}{2} \|\Omega P - Y\|_F^2 \right] &= 0 \\ \Leftrightarrow C\Omega + [\Omega P - Y]P^T &= 0 \\ \Leftrightarrow \Omega[CI + PP^T] &= YP^T \\ \Leftrightarrow \Omega &= YP^T[CI + PP^T]^{-1}. \end{aligned} \quad (5)$$

Once Ω is found, the expressions of $\Theta \in \mathbb{R}^{N \times \bar{m}}$ and $b \in \mathbb{R}^{N \times 1}$ are also known which leads to the following vector-valued function to map a feature vector into the low-dimensional subspace:

$$\rho(x_i) = \Theta k(x_i^T, B^T)^T + b. \quad (6)$$

A test pattern $x \in \mathbb{R}^n$ is assigned to a class j ($j = 1, \dots, N$) by comparing its Mahalanobis distance from the respective class centroids $\bar{\rho}^{(j)} = (1/m_j) \sum_{i=1}^{m_j} \hat{\rho}(x_i)$, i.e.,

$$\text{Class}(x) = \arg \min_{1 \leq j \leq N} d_M(\hat{\rho}(x_i), \bar{\rho}^{(j)} | \hat{\Sigma}) \quad (7)$$

where $\hat{\Sigma} = \sum_{j=1}^N (m_j - 1) \hat{\Sigma}^{(j)} / (m - N)$ is the pooled within-class covariance matrix and d_M is the Mahalanobis distance.

IV. MAIN RESULTS: AUTOMATED DEFECT DETECTION SCHEME

In this section, the schematic of the automatic surface defect detection system, feature extraction technique, training procedure, and the comparison and analysis of the experimental results are described.

A. Top Surface Inspection System Schematic

A schematic of the developed surface inspection system is shown in Fig. 1. This system is installed after the finishing stand. The thickness and length of the input slab to hot-rolling mill (HRM) may vary from 170 to 220 mm and from 9800 to 10320 mm, respectively. The output sheet thickness from

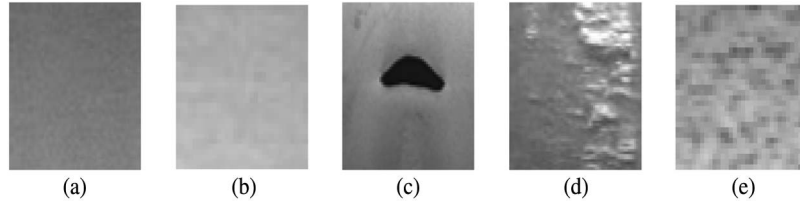


Fig. 2. Training samples of 32×32 pixels. (a) and (b) Normal samples, (c) local defect, and (d) and (e) distributed surface defect type of samples.

HRM varies from 1.5 to 12 mm. Depending on the required sheet thickness, the rolling speed of the sheet varies from a minimum of 3 m/s to the maximum capacity of the mill of 20 m/s. The temperature of the surface varies from 700 °C to 900 °C. The surface of the hot-rolled steel surface is scanned by two area scanner cameras which are mounted in a Z-frame structure. The mounting structure consists of camera housing, light holding arrangement, a wheel-mounted frame rail assembly, and shock/vibration absorbing foundation. The height of this assembly may vary from 1800 to 2400 mm from the strip with a step of 100 mm to fine-tune the positioning of camera and light control unit.

A proper arrangement is provided for the lamps to obtain a horizontal travel of 350 mm with a step of 50 mm along the length and width of the strip. The movement can be adjusted manually. The two cameras can scan the width of 1024 mm. This covers the 1000-mm-wide steel surface along with the allowance of 5 mm on either side. A lateral overlap of 10 mm among camera footprints is taken care in preprocessing of the acquired images. The allowance of 5 mm (on both sides) has been kept to incorporate the process variation of the width which is typically $1000 \pm 0.5\%$ mm. The numbering scheme of the grabbed image provides the correspondence of its physical location on the steel surface. The cameras used here are made by DALSA with the model number Pantera TF1M60A. It has a resolution of 1024×1024 pixels with maximum rate 60 frames/s and 2×40 MHz data rate. A light control unit provides the illumination of the surface by stroboscopic mechanism for small duration while taking the snapshot by the cameras. The lamps are made by Unilux, Inc. It has a flash duration of $10 \mu\text{s}$ and provides light of 1070 lx from a distance of 1200 mm. The acquisition and processing of surface image of the steel surface are performed by Matrox-made Matrox Odyssey Xpro++ media processor along with the Camera Link frame grabber. It contains 133-MHz 64-b processor with 4-GB main memory and a coprocessor memory of 64 MB, and it is 64-b peripheral component interconnect express compatible. The size of the captured image is set as 512×512 with 256 gray levels with a resolution of approximately 1 mm^2 mapped in one pixel. Thus, the system is able to detect the surface defect of size greater than approximately 2 mm^2 , which is the resolution of the system. The function of the top surface inspection system is to capture the images and to perform basic preprocessing using application programming interface of Matrox Image Library. The preprocessed annotated images are sent to the host workstation at the control room via fiber-optic link for next-level diagnosis via management information systems.

B. Feature Extraction

One of the important tasks of any machine-vision-based system is the extraction of features. If the patterns in the feature space are widely and linearly separable, then the performance of the classifier improves. The popular texture-based features are mean, standard deviation, third moment, uniformity, and entropy, described in [21]. These features perform well in case of homogeneous defects. It is difficult to classify the defects of large variation with these features. Keeping these things in mind, we have searched a set of features that can provide optimum performance for this problem. In order to support near-real-time operation, the feature extraction steps need to be computationally attractive in terms of the number of features and nature of algorithms. Therefore, defect detection algorithm should make a tradeoff between the processing time and the efficiency of defect detection system. Wavelet transform may be an ideal candidate to extract features from the surface defects [3], [11]. The proper choice of the mother wavelet plays a crucial role in the feature extraction. In this application, we have used Haar, Daubechies, Bior, and multiwavelet wavelets as these have been proved to be useful in signal and image processing applications [22]. The multiwavelet function considered here is based on the Geronimo, Hardin and Massopust multiscaling and multiwavelet function [23]. In order to investigate the minimum number of decomposition levels of the images, we have evaluated the performance of these wavelet features into three decomposition levels.

To localize the position of defects, the surface image is divided into nonoverlapping 32×32 pixel block. This selected window size is a compromise between the detection accuracy of small defects and the number of levels employed in wavelet decomposition. To construct the training set, the 32×32 pixel blocks are cropped from both the defect-free and defective images. As a result, these samples represent all types of normal and defective surfaces. A few typical representative training samples (32×32 pixel) are shown in Fig. 2. In the training phase, the feature vectors are extracted from normal 32×32 pixel blocks and are assigned to a class label -1 . The (feature) vectors, extracted from the defective 32×32 samples, are assigned to a class label $+1$.

In order to extract the features from these small-sized (32×32 pixel) images, we have used discrete wavelet transform (DWT) as it provides a powerful insight about the spatial frequency characteristics in both horizontal and vertical directions. In 2-D DWT, the transformed coefficient becomes two variable functions. Accordingly, the scaling and wavelet functions are two variable functions, denoted by $\varphi(x, y)$ and

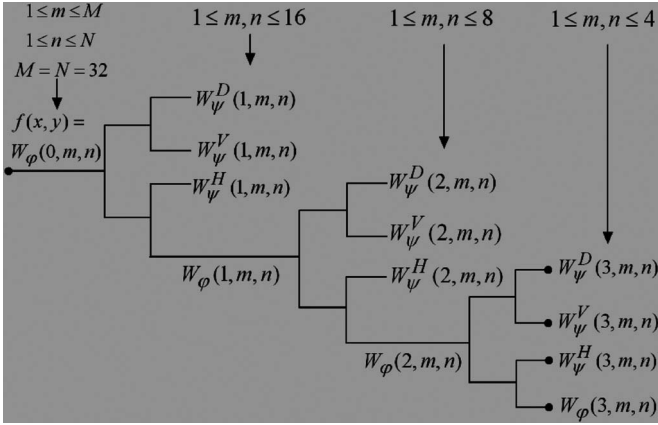


Fig. 3. Wavelet decomposition of 32×32 pixel image into three levels by DWT.

$\psi(x, y)$, respectively. The scaled and translated basis functions are defined as

$$\varphi_{j,m,n}(x, y) = 2^{\frac{j}{2}} \varphi(2^j x - m, 2^j y - n) \quad (8)$$

$$\psi_{j,m,n}^i(x, y) = 2^{\frac{j}{2}} \psi^i(2^j x - m, 2^j y - n), i = \{H, V, D\}. \quad (9)$$

Theoretically, the scaling function is the low-frequency component of the previous scaling function in two dimensions. Therefore, there is only one 2-D scaling function. There are three different wavelet functions, namely, $\psi^H(x, y)$, $\psi^V(x, y)$, and $\psi^D(x, y)$. The corresponding transformed coefficients are obtained by the equations

$$W_{\varphi}(j_0, m, n) = \frac{1}{\sqrt{MN}} \sum_{x=0}^{M-1} \sum_{y=0}^{N-1} f(x, y) \varphi_{j_0, m, n}(x, y) \quad (10)$$

$$W_{\psi}^i(j, m, n) = \frac{1}{\sqrt{MN}} \sum_{x=0}^{M-1} \sum_{y=0}^{N-1} f(x, y) \psi_{j, m, n}^i(x, y), \quad j > j_0. \quad (11)$$

Here, $f(x, y)$ is the input image of size $M \times N$, W_{φ} is the approximation coefficient, and W_{ψ}^i , for $i = H, V, D$, denotes horizontal, vertical, and diagonal detail coefficients, respectively. The input image can be viewed as approximation coefficient with order j , i.e., $f(x, y) = W_{\varphi}(j, m, n)$. The next levels of approximation and detail coefficients are obtained by (10) and (11). The three detail coefficients represent the characteristics of the image and energy at higher frequencies. On the other hand, the approximation coefficients represent the blurred version of the original image. It provides an insight about the average brightness of the image. In order to develop the illumination-invariant system, we have developed feature sets from the detail coefficients (only), at each level.

An iterative computational approach to the DWT [21], [22] is shown in Fig. 3. The filter bank decomposes the input image into four lower resolution (or lower scales) components in each pass. In the successive iteration, the approximation coefficient is again passed through the filter banks to generate the detail and approximate coefficients in the next resolution levels. In this way, we have decomposed the 32×32 pixel input sample

image into three levels and extracted the detail coefficients. Fig. 3 shows that the input image $f(x, y)$ of size 32×32 pixel represents the first resolution levels, i.e., $W_{\varphi}(0, m, n)$. The sizes of the images in the next three stages are 16×16 , 8×8 , and 4×4 pixels, respectively. To form the feature vector, the Frobenius norm $\|\bullet\|_F$ [20] of horizontal, vertical, and diagonal components of each level is considered as it represents the energy of that level. These energy levels constitute three elements of a feature vector. Thus, the elements of the feature vector is computed by concatenating the Frobenius norm of W_{ψ}^H , W_{ψ}^V , and W_{ψ}^D of different resolution levels, i.e., $FV = [\|W_{\psi}^H(j, m, n)\|_F, \|W_{\psi}^V(j, m, n)\|_F, \|W_{\psi}^D(j, m, n)\|_F]^T_{j=1,2,3}$.

When $j = 1$, the feature set consists of three elements taking the Frobenius norm of detail coefficients of level 1 only. If $j = 2$, the feature vector consists of six elements taking both level 1 and level 2 coefficients. Finally, if $j = 3$, the feature vector is of nine elements considering the coefficients of all the three levels, with three directional coefficients in each level. In this way, we have tested the performance of Haar, DB2, DB4, Bior, and multiwavelet wavelets in different decomposition levels to judge the number of resolution levels that are sufficient for this defect detection application. In addition, we have evaluated the performance of the texture-based segmentation and thresholding technique. For the texture-based segmentation, six features, such as mean, variance, smoothness, third moment, uniformity, and entropy, are extracted from the same 32×32 pixel blocks. In order to compute the performance of the threshold-based techniques, the gray-level variance of 32×32 pixel block has been compared with the preset value. The defect is implied by the variance larger than this preset threshold.

C. Training of the Classifiers

In order to train both SVM and VVRKFA, 32×32 pixel blocks of 125 defect-free image samples were randomly cropped from several images to form the training set. The same procedure is applied to generate 25 defective samples. These defective samples (32×32 pixel block) are cropped from the original defective images, independently marked by two personnel from the steel plant. These represent the complete variations of the texture of normal and defective surfaces. A Gaussian kernel [19] of the form $k(x_i, x_j) = \exp(-\mu \|x_i - x_j\|^2)$ is selected for testing the performance of both the classifiers. In our application, we have used LIBSVM toolbox [24] for the implementation of SVM classifier. All the features are normalized between zero and one before training. The same procedure is followed to normalize the test data. The parameters of the classifiers are determined by the cross-validation testing on a tuning set [25]. The optimal regularization parameters C for SVM and VVRKFA are chosen from the sets $\{2^i | i = -2, -1, \dots, 15\}$ and $\{10^i | i = -6, -5, \dots, -1\}$, respectively. The kernel parameter μ for both methods is selected from the same set $\{0.1, 0.2, \dots, 1, 2, \dots, 32\}$. Based on the cross-validation performance, the regularization parameters C and kernel parameter μ of the SVM and VVRKFA are selected separately for each individual feature sets.

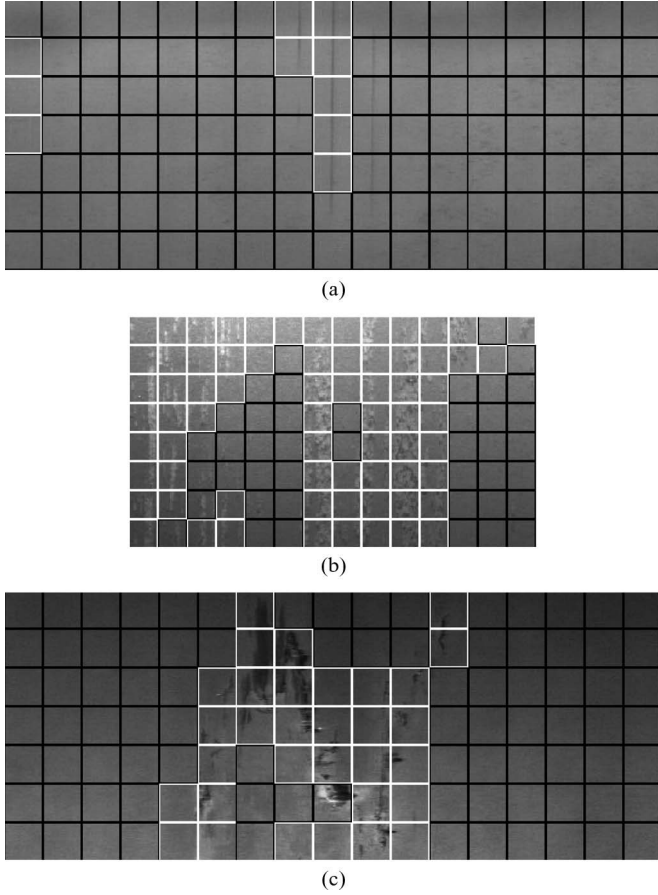


Fig. 4. Output results obtained by VVRKFA on (a) dark scratch, (b) rolled in scale, and (c) *M*-defect types of defective images using three-level Haar features. Defective blocks are marked by white perimeter, and normal blocks are marked by dark perimeter. These are cropped version of original large images.

D. Experimental Results

In this section, we have shown the experimental results and provided a comparison of performance between the SVM and VVRKFA on different sets of feature vectors for defect detection. The test feature vectors have been extracted from each of the contiguous 32×32 pixel blocks of the preprocessed test images. We have evaluated the performance of both the classifiers on 432 defective images with 24 defect types and 1000 defect-free images. In Fig. 4, we have shown typical output images obtained by VVRKFA using three-level Haar features for three defective images. The test images have blocks of both normal and defective samples. The blocks exhibiting the signature of any defect are marked by white boundary. Dark boundary is used to represent the blocks having normal signature.

In the case of defect detection application, accuracy (only) is not an appropriate performance measure of a classifier on a particular feature set. In such application, the classifier should have both low false-positive (FP) rate and false-negative (FN) rate. In order to cope with this, we have selected *G*-mean and *F*-measure as the performance evaluation metrics in this study. To define these measures, the following four metrics are first

derived from the true positive (TP), true negative (TN), FP, and FN [24]

$$\text{TP rate (TPr)} = \frac{\text{TP}}{\text{TP} + \text{FN}}$$

$$\text{TN rate (TNr)} = \frac{\text{TN}}{\text{TN} + \text{FP}}$$

$$\text{Precision} = \frac{\text{TP}}{\text{TP} + \text{FP}}$$

$$\text{Recall} = \frac{\text{TP}}{\text{TP} + \text{FN}}.$$

The *G*-mean and *F*-measure are defined as

$$G\text{-mean} = \sqrt{\text{TPr} \times \text{TNr}}$$

$$F\text{-measure} = \frac{2 \times \text{Precision} \times \text{Recall}}{\text{Precision} + \text{Recall}}.$$

G-mean measures the accuracy of both the classes in a combined way. The large value of *G*-mean indicates both high TPr and TNr, which is desirable in defect detection application. On the other hand, a large value of *F*-measure indicates small FP and small FN for a given TP.

In Table I and Table I(A) (see supplemental material, available at <http://ieeexplore.ieee.org>), we have provided the computational results obtained by SVM and VVRKFA using different wavelet feature sets on 24 different types of defective images. For example, the first row of Table I shows the experimental results obtained on 16 light scratch type of defective images. The *G*-mean and *F*-measure of SVM and VVRKFA are given in different columns considering features of Haar, DB2, and DB4 in one, two, and three levels, respectively. The best *G*-mean and *F*-measure values offered by a particular feature–classifier combination are given in boldface. In the example of light scratch type of defect, the performance of SVM with two-level Haar features is the best among all the combinations of classifiers and feature sets. From both Table I and Table I(A), it is observed that the performances of both SVM and VVRKFA with only one-level features are outperformed as compared to those with two- or three-level feature sets. Although the performance of two-level feature sets is better than that of one-level feature sets, it is not competitive with that of three-level feature sets considering either SVM or VVRKFA. This result can be explained from the fact that the features of the defect components are dominant in high frequencies. Therefore, to achieve the best detection performance, we require the wavelet coefficients of three decomposition levels. Additionally, the final rows of both Table I and Table I(A) show the overall performance of SVM and VVRKFA in defect localization. This shows that the performance depends upon the feature and classifier combination.

For better understanding, we have provided the graphical representation of percentage *G*-mean by SVM and VVRKFA using three-level feature sets of all the wavelet features along with the texture-based segmentation and thresholding in Fig. 5. From Fig. 5(a) and (b), it is observed that the performance of Haar and Bior wavelets is competitive and better than that of

TABLE I
COMPARISON OF PERCENTAGE *G*-MEAN AND *F*-MEASURE OF DEFECT DETECTION BY SVM AND VVRKFA OBTAINED EXPERIMENTALLY ON DIFFERENT TYPES OF SURFACE DEFECT IMAGES USING DIFFERENT SETS OF FEATURES

Surface defect type (No. of defective images)	Classifier	Performance of 3-level features with						Performance of 2-level features with						Performance of 1-level features with					
		Haar		DB2		DB4		Haar		DB2		DB4		Haar		DB2		DB4	
		G-mean	F-measure	G-mean	F-measure	G-mean	F-measure	G-mean	F-measure	G-mean	F-measure	G-mean	F-measure	G-mean	F-measure	G-mean	F-measure	G-mean	F-measure
Light scratch (16)	SVM	83.3	79.7	82.4	80.8	79.1	78.3	83.8	80.3	77.7	75.9	77.4	75.9	69.3	62.8	66.4	60.7	46.1	34.7
	VVRKFA	77.0	72.3	76.3	73.0	75.0	71.7	73.0	67.2	69.9	65.1	66.3	60.7	59.1	50.5	60.1	52.9	37.1	23.9
Dark scratch (16)	SVM	91.3	78.1	88.8	72.3	89.8	70.1	90.1	74.5	87.0	70.1	85.8	65.1	82.2	60.2	80.4	57.5	73.1	51.6
	VVRKFA	90.9	82.4	88.3	79.7	85.5	76.2	90.2	80.0	88.1	81.3	87.2	73.8	85.4	68.4	83.8	63.5	75.5	57.3
Head mark (14)	SVM	98.2	95.2	94.6	83.3	96.3	87.9	97.6	94.5	93.7	84.2	95.7	88.6	95.7	92.6	93.7	84.9	92.1	83.9
	VVRKFA	96.3	93.3	94.1	87.2	95.8	91.6	96.0	93.8	93.8	87.6	93.1	89.9	95.5	93.7	91.1	77.4	93.0	89.3
Heavy Scale (14)	SVM	70.0	93.5	63.3	95.4	57.2	92.6	77.4	94.2	58.6	95.0	58.2	94.4	67.7	95.7	67.4	95.3	91.7	96.9
	VVRKFA	78.7	91.9	81.7	95.6	79.9	83.3	76.1	84.8	83.8	94.4	82.4	89.4	77.2	89.9	68.2	90.9	91.3	93.6
Longitudinal crack (20)	SVM	95.8	85.4	92.0	81.4	91.9	84.0	96.8	91.4	86.2	68.7	90.1	76.1	55.3	40.2	52.9	38.7	48.2	37.1
	VVRKFA	97.4	93.7	93.2	93.0	89.5	86.1	95.2	88.9	92.6	90.4	88.8	80.0	72.0	49.3	57.8	40.7	69.0	47.1
Massive rupture (16)	SVM	95.5	94.3	96.2	94.8	98.4	97.4	98.3	97.3	96.2	94.8	90.1	88.7	95.6	94.4	80.1	76.9	69.2	64.4
	VVRKFA	97.1	95.5	95.4	93.9	92.0	90.7	96.7	94.6	93.0	91.9	92.7	91.1	90.1	88.0	84.2	82.4	67.3	61.9
M-defect (18)	SVM	89.4	65.7	88.2	62.4	88.7	64.8	89.9	66.7	89.9	65.7	86.2	61.3	90.0	70.2	86.0	62.1	76.0	62.9
	VVRKFA	91.7	77.0	91.9	77.5	85.3	72.6	91.2	76.7	90.0	76.2	83.3	68.7	85.2	69.5	86.3	62.7	79.3	71.9
Blister (14)	SVM	99.6	99.1	100	100	99.3	98.1	99.6	99.1	100	100	99.6	99.1	100	100	99.6	99.1	99.1	99.0
	VVRKFA	99.6	99.1	100	100	99.6	99.1	99.6	99.1	100	100	100	100	100	100	99.6	99.1	99.1	99.0
Bruise (14)	SVM	92.6	72.7	88.1	65.7	93.4	77.1	95.8	81.0	86.4	61.2	91.0	71.9	67.8	38.2	77.1	40.2	63.6	36.0
	VVRKFA	94.4	84.4	92.6	77.3	93.2	79.3	93.7	84.9	89.7	74.8	88.9	67.7	79.7	50.9	86.0	63.2	76.3	46.1
Rolled in dust (16)	SVM	96.4	91.7	93.7	80.0	92.8	77.0	95.5	91.0	92.9	77.5	87.4	64.2	87.8	78.8	87.6	75.7	84.0	76.4
	VVRKFA	93.8	91.2	93.6	87.9	90.2	83.7	93.1	91.1	91.9	85.5	89.4	82.8	88.0	82.3	87.2	75.0	84.1	80.0
Rolled in scale (18)	SVM	92.5	93.7	84.9	88.7	92.1	92.7	94.4	95.2	88.3	90.8	89.2	89.6	85.6	89.1	88.1	90.5	94.8	94.8
	VVRKFA	95.3	95.4	94.7	95.4	92.6	92.4	95.4	95.3	93.4	94.4	90.6	90.3	93.5	94.0	83.6	87.7	94.0	93.9
Roll mark (18)	SVM	93.0	88.1	95.0	87.6	96.7	86.3	95.2	88.6	98.1	94.3	97.1	88.2	91.6	85.7	94.1	88.4	95.7	91.8
	VVRKFA	92.3	90.0	93.5	91.4	92.3	90.0	91.0	88.6	91.0	88.6	92.1	88.9	88.5	86.8	86.7	82.1	88.5	86.8
Sagger (18)	SVM	95.9	81.5	96.7	75.6	93.9	73.6	95.9	81.5	95.8	79.5	94.6	68.8	90.8	52.9	90.3	50.4	74.9	45.7
	VVRKFA	93.6	86.1	95.1	87.7	92.2	85.7	93.5	84.9	93.3	84.5	93.4	83.8	89.3	58.3	83.2	35.1	68.6	49.3
Salt and pepper (20)	SVM	75.9	94.1	62.2	90.8	92.9	94.9	89.6	96.5	52.0	89.8	71.5	92.8	34.5	87.6	44.8	87.8	24.6	87.7
	VVRKFA	96.7	97.7	72.9	92.3	85.4	87.7	94.0	93.8	72.9	92.3	80.9	90.9	42.1	87.8	41.7	86.9	44.8	86.8
Scale grain (22)	SVM	85.0	91.8	79.0	89.5	90.8	89.0	86.1	92.3	83.6	90.9	80.4	89.0	69.8	82.1	68.5	78.5	73.1	71.9
	VVRKFA	91.6	94.6	89.9	93.5	86.6	88.3	89.7	92.6	88.5	91.6	85.1	86.1	68.5	79.6	62.5	80.0	76.4	74.5
Scale pits (18)	SVM	94.4	86.1	96.1	91.1	91.1	80.7	92.1	82.9	95.4	88.3	91.3	81.7	93.8	87.9	93.6	87.2	87.1	81.9
	VVRKFA	93.7	90.1	93.5	91.8	91.8	88.4	93.2	89.9	92.4	91.5	91.2	88.3	88.9	85.3	90.9	87.1	86.8	83.5
Seam (20)	SVM	93.7	77.6	92.7	75.8	90.4	73.1	93.6	77.3	90.8	73.3	86.4	63.3	87.9	64.8	85.7	62.0	76.4	51.4
	VVRKFA	93.7	79.6	92.2	79.6	89.9	77.0	92.1	78.0	91.0	72.9	61.0	19.8	87.1	66.4	85.7	62.0	76.4	51.4
Slab edge (18)	SVM	60.3	90.5	75.9	93.5	73.9	93.0	71.8	92.6	67.4	91.7	75.1	92.5	60.3	90.5	74.7	91.9	88.4	92.2
	VVRKFA	94.9	98.0	86.6	95.7	92.0	96.4	91.8	96.0	85.7	94.6	87.0	94.6	87.4	95.1	70.3	90.6	89.9	91.5
Spall (18)	SVM	82.8	69.6	87.0	74.7	90.4	80.0	83.8	70.8	84.2	70.8	86.5	74.0	85.9	73.6	82.2	68.6	80.3	66.4
	VVRKFA	91.0	83.6	90.2	80.4	86.7	78.1	91.0	84.3	91.0	82.0	87.6	77.8	90.4	83.0	86.9	75.5	85.1	72.7
Waviness (22)	SVM	72.7	68.8	75.1	71.4	69.8	63.9	79.1	76.6	64.4	58.3	53.9	43.8	80.2	74.4	83.3	77.5	41.5	29.4
	VVRKFA	73.2	69.5	53.6	44.6	48.4	37.7	78.4	75.6	48.8	38.4	39.3	26.6	80.3	74.3	68.8	64.8	37.3	24.5
Whip (20)	SVM	91.9	90.9	97.6	95.3	89.6	83.7	96.0	93.0	98.0	96.5	88.7	83.3	90.9	89.7	95.2	92.9	69.0	64.5
	VVRKFA	96.8	95.2	96.4	94.1	78.1	74.3	89.1	84.3	95.7	94.1	72.1	67.7	78.0	69.1	90.2	87.5	63.6	57.6
Deposits (28)	SVM	99.3	99.3	98.9	97.1	99.3	98.2	98.3	97.0	98.4	96.0	98.4	94.6	97.8	96.3	99.1	98.2	88.9	87.1
	VVRKFA	99.3	99.3	99.2	98.5	99.2	97.1	91.8	89.1	98.7	97.4	98.8	96.4	87.9	83.3	98.7	97.4	93.6	89.3
Sticker Break (24)	SVM	90.1	82.9	93.3	87.5	92.1	85.7	91.3	95.6	91.3	84.6	91.3	84.9	83.7	92.3	92.1	85.7	90.9	84.0
	VVRKFA	94.4	89.4	92.9	87.3	98.2	96.2	94.0	96.9	94.8	90.0	94.4	89.9	86.6	93.5	91.0	84.7	96.3	93.2
Damage (10)	SVM	93.1	96.4	93.1	96.4	86.6	93.5	90.5	44.4	98.0	99.1	79.8	86.9	92.5	50.0	80.6	91.1	64.9	78.2
	VVRKFA	96.6	98.2	94.0	96.9	42.8	45.6	90.3	56.3	92.2	96.0	87.0	91.3	78.3	41.2	80.6	91.1	61.2	77.9
Overall performance	SVM	93.0	87.0	93.5	87.8	88.7	79.1	92.5	85.3	91.6	84.3	87.4	77.5	91.1	85.2	89.2	80.6	81.1	71.6
	VVRKFA	93.8	90.4	92.0	88.3	87.9	80.2	92.7	88.5	91.5	87.1	86.9	76.8	87.2	83.1	87.4	82.4	81.9	74.2

other wavelets and texture-based segmentation or thresholding. This can be explained by the fact that the Haar wavelet has good space localization but poor frequency localization. In

defect detection application, we need the spatial localization of the defects rather than the frequency localization property. Moreover, the extraction of Haar wavelet features is

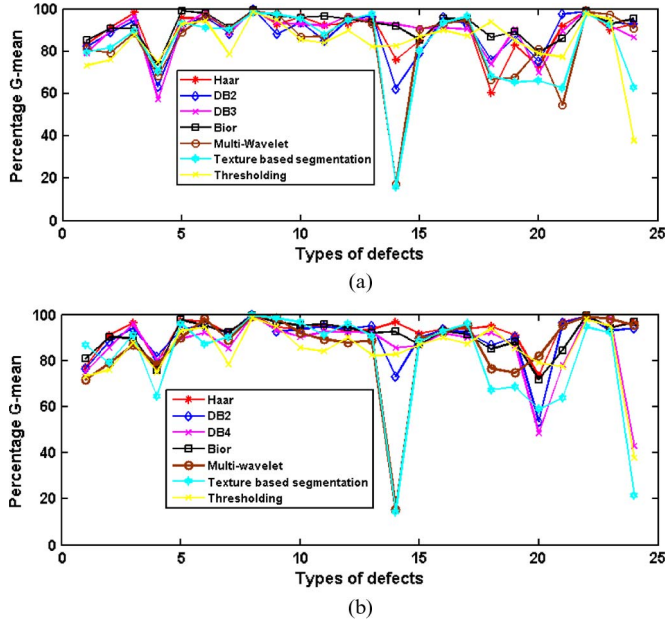


Fig. 5. Variation of percentage G -mean using three resolution levels of Haar, DB2, DB4, Bior, and multiwavelet feature sets. Texture-based segmentation along with thresholding for different types of defects by (a) SVM and (b) VVRKFA.

computationally cost effective. Additionally, it is observed that the performance of VVRKFA may be slightly better than that of SVM classifier.

In this defect detection application, wavelet coefficients have been used for the characterization of localized anomalies (either in space domain or in frequency domain) in observed images. Most of the surface defects produce a change in normal homogeneous surface texture of steel strips. The patterns created by the inhomogeneous regions depend on the types of the defects. The disturbances in the intensity distribution can be localized in a small zone, can be distributed almost all throughout in a semiperiodic fashion, or can be oriented in a particular direction depending on the types of defect. DWT has a better ability in localizing these characteristics in both space and frequency domains. A simple and powerful feature extracted from the wavelet coefficients is the total energy of each detail image. This is defined as the sum of the squares of coefficients of each detail image obtained by wavelet transform. Such energy signatures provide a good indication of the total energy contained at specific spatial frequency levels and orientations. The differences between the normal and defect surface blocks are being detected by analyzing these energy signatures with the help of a pattern classification algorithm.

The accuracy of the detection of normal samples is also equally important in case of an automated system. The testing results on 1000 normal images are shown in Table II separately. From Table II, it is observed that all the wavelet feature sets are almost equally able to detect the defect-free 32×32 pixel blocks. In this case, even one-level Haar, DB2, DB4, Bior, and multiwavelet features can produce the classification accuracy similar to that of the two- or three-level features. However, it is observed that texture-based segmentation and thresholding techniques offer a little less accuracy owing to more FP figures.

These results also support the need of wavelet-based features in this defect detection application.

The evaluation of the processing time of the proposed method is as follows: The resolution of the captured image has been set to 512×512 pixel to reduce the effect of minute variation (in gray level) and the computational burden. Since the developed diagnostic platform captures $1 \times 1 \text{ mm}^2$ of the surface in one pixel, a 512×512 pixel image covers $512 \times 512 \text{ mm}^2$ of width of the strip. The two cameras cover the 1000 mm width of the strip along with the allowance of 5 mm on both sides. The portion of the captured images outside the boundary of the steel surface (i.e., 5 mm on each side) is removed at preprocessing level. Thus, for a 100-m-long surface, there will be approximately 400 ($100/0.5 \times 2$) images. Each of the two Dell 690 workstations processes 200 images. Table III shows the time requirements in seconds to test a 100-m-long steel surface using three-level wavelet feature set and classifier combination along with texture segmentation and thresholding technique. The average has been taken over 100 runs. The necessary operations are division of image into nonoverlapping contiguous 32×32 pixel blocks, feature extraction, and testing by the algorithms. It is observed that the texture segmentation and thresholding techniques take less time compared to all the wavelet feature sets. However, as the wavelet features performed better (in terms of accuracy) than these two techniques, we have to consider them for timing calculation. Therefore, to test 200 images in each of the two Dell 690 workstations, VVRKFA and SVM need approximately 17.3 and 16.4 s, respectively, with three-level Haar features. It is observed from Table III that, as the number of decomposition level decreases, the testing time also decreases. This timing analysis shows that the proposed algorithm guarantees the feasibility of the real-time processing with three-level feature sets with the rolling speed restricted to 5 m/s. With this assumption, 100-m traversal of the sheet requires $100/5 = 20$ s, and within this time, the defect detection calculations will be completed.

V. CONCLUSION

The central outcome of this paper is that the wavelet feature sets are better suitable for steel surface defect detection application compared to texture-based segmentation or thresholding techniques. Further, three-level Haar feature set is more promising compared to the Daubechies, Bior, and multiwavelet wavelet features. The limitation of this method is that if the speed of the rolling is greater than 5 m/s, it is difficult to process in real time (with the existing hardware setup) but may be processed in near real time. Also, we have not considered that the noise appears due to the uneven illumination and vibration of the sheets during the image acquisition. A major concern in surface inspection system is the presence of the specular reflections. For a few types of defects, such as waviness, damages, etc., the deformation induces reflection. This leads to increase in FP near the defective region. The construction of the training set is also challenging in this application. The training set should span the signature of all types of defects and that of normal surface. The future work includes the improvement of

TABLE II
PERCENTAGE ACCURACY BY SVM AND VVRKFA OBTAINED EXPERIMENTALLY ON DEFECT-FREE IMAGES USING DIFFERENT SETS OF FEATURES

Image type	Classifier	Performance of 3-level features with					Performance of 2-level features with					Performance of 2-level features with					Texture based segmentation	Thresholding
		Haar	DB2	DB4	Bior	Multi-wavelet	Haar	DB2	DB4	Bior	Multi-wavelet	Haar	DB2	DB4	Bior	Multi-wavelet		
Defects free (1000)	SVM	99.68	99.65	99.64	99.69	99.63	99.64	99.62	99.58	99.67	99.61	99.60	99.54	99.56	99.66	99.60	95.48	98.63
	VVRKFA	99.70	99.64	99.65	99.67	99.62	99.66	99.65	99.53	99.65	99.64	99.61	99.57	99.51	99.65	99.62	97.73	

TABLE III
COMPARISON OF AVERAGE TESTING TIME IN SECONDS BY VARIOUS FEATURE SETS AND CLASSIFIER COMBINATIONS FOR 100-m-LONG STEEL SURFACE

Classifier	3 levels wavelet feature sets with					Texture segmentation	Thresholding
	Haar	DB2	DB4	Bior	Multi-wavelet		
SVM	16.4	17.5	18.6	17.6	17.4	8.7	7.6
VVRKFA	17.3	18.2	19.1	17.8	17.5	8.9	

defect detection accuracy by feature selection and combining different classifiers.

ACKNOWLEDGMENT

This work was implemented at Bokaro Steel Plant of Steel Authority of India Ltd.

REFERENCES

- [1] X. Li, S. K. Tso, X.-P. Guan, and Q. Huang, "Improving automatic detection of defects in castings by applying wavelet technique," *IEEE Trans. Ind. Electron.*, vol. 53, no. 6, pp. 1927–1934, Dec. 2006.
- [2] R. Stojanovic, P. Mitropoulos, C. Koulamas, Y. Karayiannis, S. Koubias, and G. Papadopoulos, "Real-time vision-based system for textile fabric inspection," *Real-Time Imaging*, vol. 7, no. 6, pp. 507–518, Dec. 2001.
- [3] A. Kumar, "Neural network based detection of local textile defects," *Pattern Recognit.*, vol. 36, no. 7, pp. 1645–1659, Jul. 2003.
- [4] A. Kumar, "Computer-vision-based fabric defect detection: A survey," *IEEE Trans. Ind. Electron.*, vol. 55, no. 1, pp. 348–363, Jan. 2008.
- [5] S. M. Chao and D. M. Tsai, "An anisotropic diffusion-based defect detection for low-contrast glass substrates," *Image Vis. Comput.*, vol. 26, no. 2, pp. 187–200, Feb. 2008.
- [6] W.-C. Li and D.-M. Tsai, "Defect inspection in low-contrast LCD images using hough transform-based non-stationary line detection," *IEEE Trans. Ind. Informat.*, vol. 7, no. 1, pp. 136–147, Feb. 2011.
- [7] A. Mukherjee, T. Ray, S. Chaudhuri, P. K. Dutta, S. Sen, and A. Patra, "Image-based classification of defects in frontal surface of fluted ingot," *Mesurement*, vol. 40, no. 6, pp. 687–698, Jul. 2007.
- [8] T. Sugimoto and T. Kawaguchi, "Development of a surface defect inspection system using radiant light from steel products in a hot rolling line," *IEEE Trans. Instrum. Meas.*, vol. 47, no. 2, pp. 409–416, Apr. 1998.
- [9] S. H. Choi, J. P. Yun, B. Seo, Y. Park, and S. W. Kim, "Real-time defects detection algorithm for high-speed steel bar in coil," *Proc. World Acad. Sci., Eng. Technol.*, vol. 21, pp. 66–70, Jan. 2007.
- [10] P. C.-Solly and J. E. Smith, "Adaptive surface inspection via interactive evolution," *Image Vis. Comput.*, vol. 25, no. 7, pp. 1058–1072, Jul. 2007.
- [11] W. X.-Yong, X. Ke, and X. J.-Wu, "Application of undecimated wavelet transform to surface defect detection of hot rolled steel plates," in *Proc. Congr. Image Signal Process.*, Sanya, China, May 2008, pp. 528–532.
- [12] Y. Zhang, H. Zhou, S. J. Qin, and T. Chai, "Decentralized fault diagnosis of large-scale processes using multiblock kernel partial least squares," *IEEE Trans. Ind. Informat.*, vol. 6, no. 1, pp. 3–10, Feb. 2010.
- [13] C. H. Lo, E. H. K. Fung, and Y. K. Wong, "Intelligent automatic fault detection for actuator failures in aircraft," *IEEE Trans. Ind. Informat.*, vol. 5, no. 1, pp. 50–55, Feb. 2009.
- [14] M. D. Ma, D. S. H. Wong, S. S. Jang, and S.-T. Tseng, "Fault detection based on statistical multivariate analysis and microarray visualization," *IEEE Trans. Ind. Informat.*, vol. 6, no. 1, pp. 18–24, Feb. 2010.
- [15] P.-E. P. Odiwei and Y. Cao, "Nonlinear dynamic process monitoring using canonical variate analysis and kernel density estimations," *IEEE Trans. Ind. Informat.*, vol. 6, no. 1, pp. 36–45, Feb. 2010.
- [16] V. Vapnik, *The Nature of Statistical Learning Theory*. New York: Springer-Verlag, 1995.
- [17] N. Cristianini and J. Shawe-Taylor, *An Introduction to Support Vector Machines*. Cambridge, MA: Cambridge Univ. Press, 2000.
- [18] S. Ghorai, A. Mukherjee, and P. K. Dutta, "Discriminant analysis for fast multiclass data classification through regularized kernel function approximation," *IEEE Trans. Neural Netw.*, vol. 21, no. 6, pp. 1020–1029, Jun. 2010.
- [19] N. Cristianini and J. S. Taylor, *Kernel Methods for Pattern Analysis*. Cambridge, U.K.: Cambridge Univ. Press, 2004.
- [20] G. Strang, *Linear Algebra and Its Applications*, 4th ed. Jackson, WY: Nelson Engineering, 2007.
- [21] R. C. Gonzalez and R. C. Woods, *Digital Image Processing*, 2nd ed. Upper Saddle River, NJ: Pearson Education, 2007.
- [22] S. G. Mallat, *A Wavelet Tour of Signal Processing*, 2nd ed. New York: Academic, 1999.
- [23] X.-G. Xia, J. S. Geronimo, D. P. Hardin, and B. W. Suter, "Design of pre-filters for discrete multiwavelet transforms," *IEEE Trans. Signal Process.*, vol. 44, no. 1, pp. 25–35, Jan. 1996.
- [24] C.-C. Chang and C.-J. Lin, LIBSVM: A Library for Support Vector Machines, vol. 2, no. 3, p. 27, Apr. 2001. [Online]. Available: <http://www.csie.ntu.edu.tw/~cjlin/libsvm>
- [25] T. M. Mitchell, *Machine Learning*. Singapore: McGraw-Hill, 1997.



Santanu Ghorai (S'07–M'12) received the B.Sc. degree (Hons.) in physics and the B.Tech. degree in instrumentation engineering from the University of Calcutta, Kolkata, India, in 1995 and 1998, respectively, the M.E. degree in electrical engineering from Jadavpur University, Kolkata, in 2000, and the Ph.D. degree from the Department of Electrical Engineering, Indian Institute of Technology Kharagpur, Kharagpur, India, in 2011.

He is currently with the faculty of the Department of Applied Electronics and Instrumentation Engineering, Heritage Institute of Technology, Kolkata. His main research interests include signal processing, machine learning, and bioinformatics.



Anirban Mukherjee (M'06) received the B.E.E. degree in electrical engineering from Jadavpur University, Kolkata, India, in 1998 and the M.Tech. and Ph.D. degrees in electrical engineering from the Indian Institute of Technology Kharagpur, Kharagpur, India.

In 2004–2005, he was with the Centre of Excellence for Embedded Systems, Tata Consultancy Services Ltd. He is currently with the faculty of the Department of Electrical Engineering, Indian Institute of Technology Kharagpur. His principal research

interests include signal processing and machine learning.



M. Gangadaran was born in Tamil Nadu, India. He received the B.Sc. degree in mathematics from the University of Madras, Chennai, India, the B.Tech. degree in electronics from Anna University, Chennai, and the M.E. degree in systems and control engineering from Osmania University, Hyderabad, India.

From 1984 to 1990, he was a Technical Officer with Electronics Corporation of India Ltd., Hyderabad. From 1990 to 1991, he was an Assistant Manager with the Indian Telephone Industries Ltd., Palakkad, India. Since 1991, he has been with the

AAPC Group, Research and Development Centre for Iron and Steel, Steel Authority of India Ltd., Ranchi, India. His areas of interest are system design and development of industrial process control, image processing application in steel industry, and expert system.



Pranab K. Dutta (M'10) received the B.E. and M.E. degrees in electrical engineering from the University of Calcutta, Kolkata, India, in 1984 and 1986, respectively, and the Ph.D. degree in electrical engineering from the Department of Electrical Engineering, Indian Institute of Technology Kharagpur, Kharagpur, India, in 1992.

He is with the Indian Institute of Technology Kharagpur, Kharagpur, India, where he is a member of Faculty with the Department of Electrical Engineering since 1993 and is currently the Head of the

School of Medical Science and Technology. His principal research interests include signal processing and machine learning.